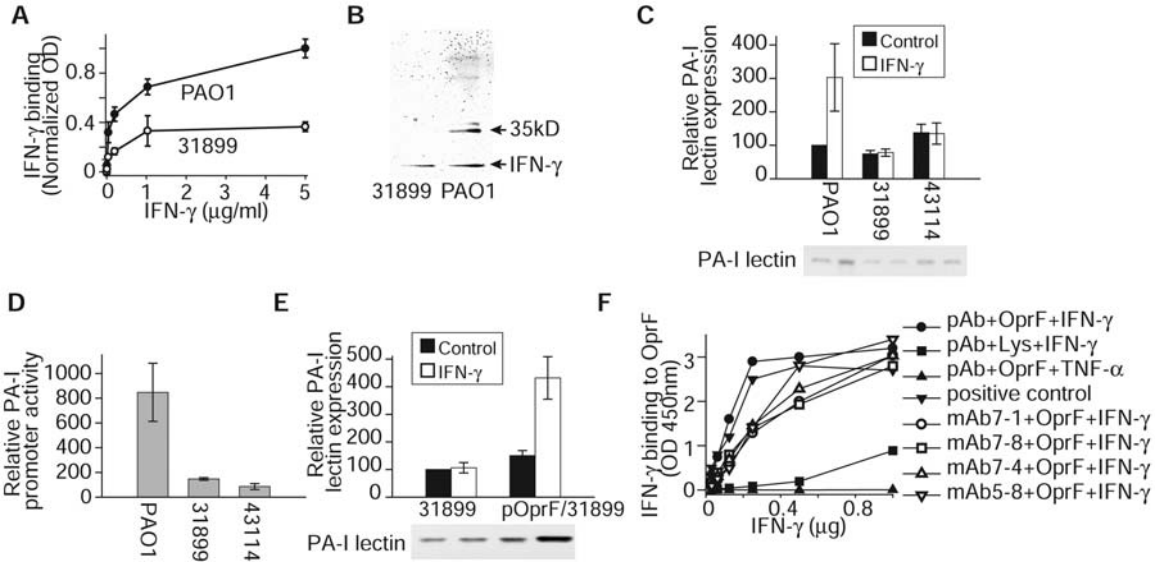

Fig. 4. IFN-γ binds to OprF and induces PA-I expression. Error bars, mean ± SD. (**A**) ELISA binding assays of IFN-γ to solubilized membrane protein from wild-type *P. aeruginosa* (PAO1) and the OprF knockout mutant strain 31899 showing attenuated IFN-γ binding to the solubilized membrane protein from the mutant strain. (**B**) Immunoprecipitation of solubilized membrane proteins from OprF mutant strain 31899 with IFN-γ, demonstrating absence of the 35-kD band seen with the parent wild-type strain (PAO1). (**C**) PA-I protein expression measured by immunoblot in wild-type (PAO1) and mutant strains (31899, 43114) exposed to 200 ng/ml IFN-γ, demonstrating an inability of IFN-γ to enhance the expression of PA-I in the OprF mutant strains. (**D**) Wild-type strain (PAO1) and OprF mutant strains (31899, 43114) carrying the GFP-PA-I fusion plasmid were incubated with 200 ng/ml IFN-γ, and fluorescence was assessed over time. Results demonstrate a lack of enhanced PA-I expression in mutants exposed to IFN-γ. (**E**) Reconstitution of OprF in mutant strain 31899 demonstrating reestablishment of the responsiveness of PA-I expression to IFN-γ. (**F**) Antibody to OprF (polyclonal, pAb; monoclonal, mAb) was coated onto microtiter plate. The complexes [OprF and IFN-γ, IFN-γ and Lys (lysozyme), and OprF and TNF-α] were added and detected by biotin-labeled antibody to IFN-γ. ELISA assay demonstrated that human IFN-γ binds to purified OprF. Results are a representative experiment of three independent studies.

necessary to confirm the role of IFN-γ binding to OprF on *P. aeruginosa* virulence in vivo.

References and Notes

1. H. Ochman, N. A. Moran, *Science* **292**, 1096 (2001).
2. J. J. Mekalanos, *J. Bacteriol.* **174**, 1 (1992).
3. R. S. Laughlin *et al.*, *Ann. Surg.* **232**, 133 (2000).
4. O. Bajolet-Laudinat *et al.*, *Infect. Immun.* **62**, 4481 (1994).
5. K. Winzer *et al.*, *J. Bacteriol.* **182**, 6401 (2000).
6. D. J. Schwartzentruber, S. L. Topalian, M. Mancini, S. A. Rosenberg, *J. Immunol.* **146**, 3674 (1991).
7. Materials and methods are available as supporting material on *Science* Online.
8. L. Wu *et al.*, *Gastroenterology* **126**, 488 (2004).
9. C. K. Stover *et al.*, *Nature* **406**, 959 (2000).
10. S. P. Diggle, K. Winzer, A. Lazdunski, P. Williams, M. Camara, *J. Bacteriol.* **184**, 2576 (2002).
11. M. Whiteley, K. M. Lee, E. P. Greenberg, *Proc. Natl. Acad. Sci. U.S.A.* **96**, 13904 (1999).
12. V. E. Wagner, D. Bushnell, L. Passador, A. I. Brooks, B. H. Iglewski, *J. Bacteriol.* **185**, 2080 (2003).
13. G. W. Lau, H. Ran, F. Kong, D. J. Hassett, D. Mavrodi, *Infect. Immun.* **72**, 4275 (2004).
14. A. O. Azghani, S. Idell, M. Bains, R. E. Hancock, *Microb. Pathog.* **33**, 109 (2002).
15. M. A. Jacobs *et al.*, *Proc. Natl. Acad. Sci. U.S.A.* **100**, 14339 (2003).
16. R. Porat, B. D. Clark, S. M. Wolff, C. A. Dinarello, *Science* **254**, 430 (1991).
17. G. Luo, D. W. Niesel, R. A. Shaban, E. A. Grimm, G. R. Klimpel, *Infect. Immun.* **61**, 830 (1993).
18. S. Ikuta *et al.*, *Shock* **21**, 452 (2004).
19. S. P. Diggle *et al.*, *Mol. Microbiol.* **50**, 29 (2003).
20. E. C. Pesci *et al.*, *Proc. Natl. Acad. Sci. U.S.A.* **96**, 11229 (1999).

21. We thank D. R. Clayburgh for assistance with the figure preparations, P. Williams and K. Winzer for providing *Escherichia coli* strain harboring the reporter plasmid pSB536, and H. P. Schweizer for providing plasmid pUCP24. J.C.A. and E.B.C. are founding members and shareholders of Midway Pharmaceuticals, which is involved in developing compounds that interfere with host compounds released during stress and bacterial receptors. This work was supported by NIH grants 2-RO1 GM062344-05 (J.C.A.); R01DK61931 and R01DK68271 (J.R.T.); DK-47722 and DK-38510 (E.B.C.); and by the Canada Research Chairs Program and the Canadian Institutes of Health Research (R.E.W.H.).

Supporting Online Material
www.sciencemag.org/cgi/content/full/309/5735/774/DC1

17 March 2005; accepted 2 June 2005
10.1126/science.1112422

A Phenylalanine Clamp Catalyzes Protein Translocation Through the Anthrax Toxin Pore

Bryan A. Krantz,[1]* Roman A. Melnyk,[1]* Sen Zhang,[1] Stephen J. Juris,[1] D. Borden Lacy,[1] Zhengyan Wu,[2] Alan Finkelstein,[2] R. John Collier[1]†

The protective antigen component of anthrax toxin forms a homoheptameric pore in the endosomal membrane, creating a narrow passageway for the enzymatic components of the toxin to enter the cytosol. We found that, during conversion of the heptameric precursor to the pore, the seven phenylalanine-427 residues converged within the lumen, generating a radially symmetric heptad of solvent-exposed aromatic rings. This "ϕ-clamp" structure was required for protein translocation and comprised the major conductance-blocking site for hydrophobic drugs and model cations. We conclude that the ϕ clamp serves a chaperone-like function, interacting with hydrophobic sequences presented by the protein substrate as it unfolds during translocation.

Anthrax toxin is composed of three nontoxic proteins, which combine on eukaryotic cell surfaces to form toxic, noncovalent complexes. [See (*1*) for a review.] Protective antigen (PA), the protein translocase component, binds to a cellular receptor and is activated by a furin-family protease. The resulting 63-kD receptor-bound fragment, PA_{63}, self-assembles into the prepore, which is a ring-shaped homoheptamer (Fig. 1A). The prepore then forms complexes with the two ~90-kD enzymatic components, lethal factor (LF) and edema factor (EF). These complexes are endocytosed and delivered to an acidic compartment (*2*). There, the prepore undergoes an acidic pH-dependent conformational rearrangement (*3*) to form an ion-

conducting, cation-selective, transmembrane pore (*4*), allowing bound LF and EF to translocate into the cytosol.

The PA_{63} pore (Fig. 1B) is believed to consist of a mushroom-shaped structure, with a globular cap connected to a β-barrel stem that is ~100 Å long (*5*, *6*). A model of the 14-strand β barrel reveals its lumen, which is ~15 Å wide and can only accommodate structure as wide as an α helix (*7*). The narrow pore creates a structural bottleneck, requiring that the catalytic factors, LF and EF, unfold in order to be translocated (*8*, *9*). The destabilization energy required to unfold the tertiary structure of LF and EF originates partly from the acidic pH in endosomes, which causes their N-terminal domains (LF_N and EF_N) to become molten globules (MG) (*7*). A positive membrane potential [$+\Delta\psi$ (*10*)], when coupled with these acidic pH conditions, is sufficient to drive LF_N through PA_{63} pores formed in planar lipid bilayers (*9*). To enter the narrow confines of the ~15-Å-wide lumen, LF_N must shed its residual tertiary structure and convert from the MG form to an extended, "translocatable" conformation (*7*). How does a solvent-filled pore mediate the disassembly of an MG protein, packed, albeit loosely, with hydrophobically dense stretches of polypeptide? We surmised that an interaction surface inside the pore might facilitate further unfolding of the MG to the extended, translocatable form.

By cysteine-scanning mutagenesis coupled to [2-(trimethylammonium) ethyl]methanethiosulfonate (MTS-ET) modification (*5*) (Fig. 1C), we identified residues that line the lumen of PA_{63} in the globular cap portion of domain 2, the pore-forming domain (Fig. 1D). F^{427} (*11*) was the most hydrophobic residue identified in the otherwise hydrophilic pore lining. It is absolutely conserved in homologous toxins (fig. S1), and mutating it blocks protein translocation (*12*, *13*). $F^{427}\rightarrow C^{427}$ (F427C) channels were most strongly affected by MTS-ET modification, implying that F^{427} is prominent and solvent-exposed within the lumen.

To address how the seven F^{427} residues were arranged within the lumen of the PA_{63} pore, we used electron paramagnetic resonance spectroscopy (EPR) to measure the proximity of nitroxide spin labels attached to F427C. The EPR spectrum of the spin-labeled prepore showed weak spin-spin interactions (Fig. 1E). This observation was consistent with the crystal structure of the prepore, in which F^{427} lies in a disordered loop (2β10 to 2β11) near the lumen, such that neighboring F^{427} residues are 15 to 20 Å apart (Fig. 1A). Upon conversion to the pore state by acidification to pH 6, a saturating spin-spin interaction appeared, indicating that the spin probes had converged and were separated by less than 10 Å (Fig. 1E). Consistent with this, single-channel ion conductances were roughly inversely proportional to the size of the substitution at 427 (Fig. 1F), as predicted from a cylindrical pore conductance model (*14*). Channels with large aliphatic (Leu) or aromatic (Trp) residues at 427 showed smaller conductances than channels with Ala or Phe, their smaller respective counterparts. Thus, as the pore forms, the seven phenylalanines create a narrow aromatic iris, or "ring of rings," within the lumen (Fig. 1B and supporting online material text).

In planar lipid bilayers, LF_N binds to wild-type (WT) PA_{63} pores, blocking ion conductance by >95% (at +20 mV and ~10 nM LF_N; Fig. 2C); the first 21 residues of LF_N's cation-rich, flexible N terminus are essential for this macroscopic blocking effect (*15*). At the single-channel level, the N terminus of LF_N bound stably within the PA_{63} channel and prevented passage of hydrated K^+ ions, as manifested by a continuously closed state (Fig. 2A). When F427A PA_{63} was similarly assayed, LF_N was only able to block macroscopic conductance by ~50% (Fig. 2C). In single-channel recordings, the partial block observed for F427A PA_{63} channels resulted from a dynamic "flickering" between an open state, multiple partly closed substates, and a fully closed state (Fig. 2A). Histogram analysis of a single-channel recording of F427A PA_{63} (Fig. 2B) was consistent with macroscopic experiments, in that the average conductance was ~50% of the open channel conductance (Fig. 2C). We infer that LF_N is bound to the domain 1′ surface of the F427A channel, but its flexible N terminus, which enters the channel first (*15*), is not stably bound within the lumen and is unable to block conductance effectively. LF_N blocked PA_{63} pores more effectively with large aromatic or aliphatic residues at position 427 than with small or hydrophilic residues (fig. S2). Thus the heptad of F^{427} residues is integral to binding LF_N's N terminus, leading us to term the site the "ϕ clamp."

To probe the role of the ϕ clamp in polypeptide translocation, we measured the rate of LF_N translocation through PA_{63} channels formed in planar lipid bilayers (*9*). LF_N was added to the cis compartment, blocking conductance. After perfusing to remove unbound LF_N, we stepped $\Delta\psi$ to a higher positive voltage and monitored the rate of translocation by the increase in channel conductance as LF_N

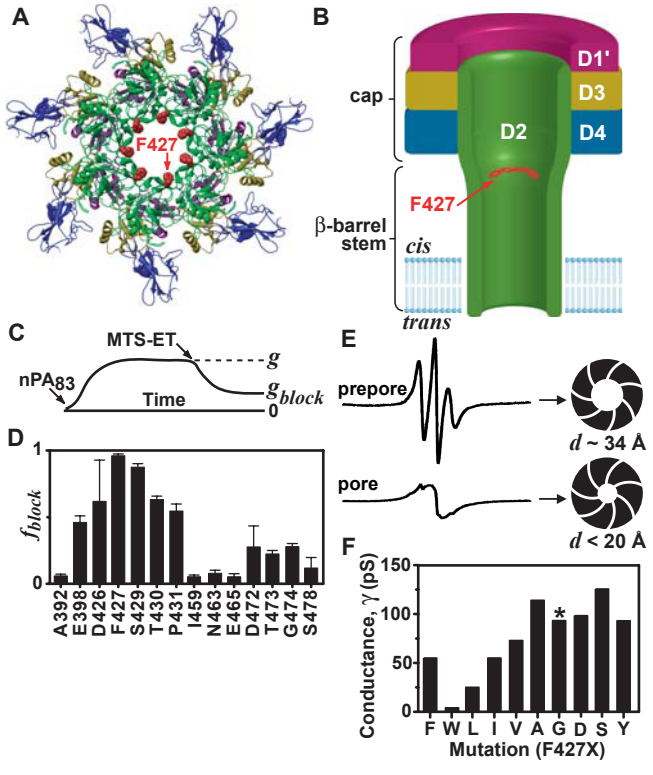

Fig. 1. Structural models of a lumen-facing phenylalanine heptad. (**A**) A ribbons rendering of the PA_{63} prepore (*27*), viewed axially, where domain 4 is proximal. Domains are colored: D1′ (magenta), D2 (green), D3 (gold), and D4 (blue). F427 (red, space filling) is modeled into the structure. (**B**) Hypothetical cross section of the PA_{63} channel, or pore, colored as in (A). The membrane-spanning tube is the 14-stranded β barrel from domain 2 (*5*, *6*). (**C**) Illustration of the effect of MTS-ET modification on Cys-substituted mutants of PA_{63} in macroscopic conductance studies. Conductance, *g*, is determined from the current, *I*, and $\Delta\psi$ as $g = I/\Delta\psi$. (**D**) Fraction of conductance blocked (f_{block}) by MTS-ET modification (*28*) in domain 2 cap residues [as in (C), where $f_{block} = 1 - g_{block}/g$] (table S2). Error bars show means + σ_{SE} ($n = 3$). (**E**) EPR spectra of PA_{63} heptamers uniformly labeled at F427C with a Cys-reactive nitroxide spin label in the prepore state at pH 8.5 (upper spectrum) and the pore state at pH 6 (lower spectrum). Approximate luminal diameters, *d*, are based on the observed spin-spin interactions. (**F**) Unitary conductance, γ, of single PA_{63} channels, with indicated substitutions at F^{427}. Channels formed by F427G PA_{63} (*) initially opened to a conductance of 90 pS, but, unlike any of the other channels, flickered to 60 and 30 pS substates. γ values are accurate to at least ±10%, except for F427L and F427W, which are accurate to ±20%.

[1]Department of Microbiology and Molecular Genetics, Harvard Medical School, 200 Longwood Avenue, Boston, MA 02115, USA. [2]Department of Physiology and Biophysics, Albert Einstein College of Medicine, 1300 Morris Park Avenue, Bronx, NY 10461, USA.

*These authors contributed equally to this work.
†To whom correspondence should be addressed. Email: jcollier@hms.harvard.edu

traversed the pore (Fig. 2D). With the most active substitutions at F^{427}, LF_N translocated at rates that trended as Phe > Leu ≈ Trp > Tyr (Fig. 2D). Other small aliphatic or hydrophilic substitutions, including Asp (an isosteric, hydrophilic control for Leu), were inefficient at promoting translocation. The most active residue, therefore, was Phe; the more hydrophilic aromatic, Tyr, was five times less active. These in vitro translocation studies recapitulated results of cellular assays of toxin action (Fig. 2E). Preference at the ϕ-clamp site for the γ-branched Leu over its β-branched isomer, Ile, correlates with the fact that aromatic residues also place more hydrophobic surface nearer to the center of the lumen. Thus the ϕ-clamp structure represents an active site, requiring either an aromatic surface or a more centrally oriented aliphatic surface to catalyze translocation efficiently.

Considering the hydrophobicity of the ϕ clamp, we hypothesized that this site may also be the binding site for hydrophobic cations, such as tetrabutylammonium (TBA) (Fig. 3A) (*16*). This hypothesis is consistent with studies suggesting that the TBA site is within the cap of the PA_{63} channel, cis to the extended β barrel (*6*). TBA's affinity for F427A channels was greatly reduced from that of WT (4000-fold, or ~5 kcal mol^{-1}; Fig. 3D). Large aliphatic residues at 427 were unable to recover the TBA block (Fig. 3E). F427L channels, for example, had a ~4 kcal mol^{-1} reduction in affinity for TBA. The least defective substitution was F427Y, which reduced the TBA block fourfold, or ~0.8 kcal mol^{-1}. The recovery of the TBA block in F427Y channels was notable, because Tyr is substantially more hydrophilic than Phe. We infer that the TBA blocking mechanism also includes cation-π

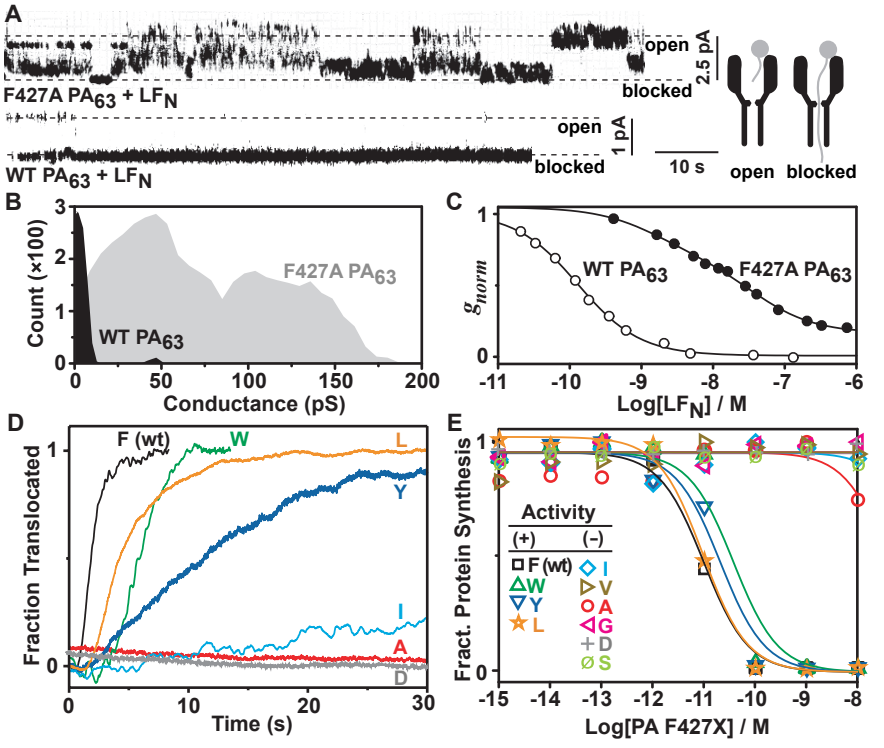

Fig. 2. LF_N conductance block and translocation studies with PA_{63} mutated at F^{427}. (**A**) Current record for a single F427A PA_{63} channel (upper panel) exhibiting partial block with 7 nM LF_N in the cis compartment. A similar single-channel record for a WT channel (lower panel) shows complete block with 7 nM LF_N in the cis compartment [Δψ = +20 mV (*10*), pH 5.5]. A diagram (right) showing the "blocked" channel corresponds to LF_N's N terminus binding within the pore. (**B**) Histogram of the single-channel conductances for the LF_N block in (A) for WT (black) and F427A PA_{63} (gray). (**C**) Concentration dependence of the LF_N conductance block for WT (○) and F427A PA_{63} channels (●) under macroscopic conditions (Δψ = +20 mV, pH 5.5). Normalized conductance (g_{norm}) curves are fitted to a single- and two-site binding model for WT and F427A channels, respectively, where the WT equilibrium dissociation constant (K_D) is ~150 pM. (**D**) Planar lipid bilayer macroscopic conductance records of LF_N translocation through WT and the indicated F^{427} mutant channels [where pH_{cis} = 5.5, pH_{trans} = 6.5 (*29*)]. After PA_{63}-induced channel formation reached steady state, 20 nM LF_N was added to the cis compartment (under a Δψ of +1 to +10 mV). When the conductance block reached steady state, the cis compartment was perfused, and translocation (as manifested by the rise in conductance) was initiated by increasing Δψ to +30 mV. Plotted records were normalized as the fraction translocated, excepting F427A and F427D channels, in which no appreciable translocation occurred. (**E**) Cellular translocation assay of F427 PA mutants (*12*), where translocation is reported by detecting the inhibition of protein synthesis by the domain from diphtheria toxin, which is fused to the C terminus of LF_N. Mutants are classified as active (+) or inactive (–).

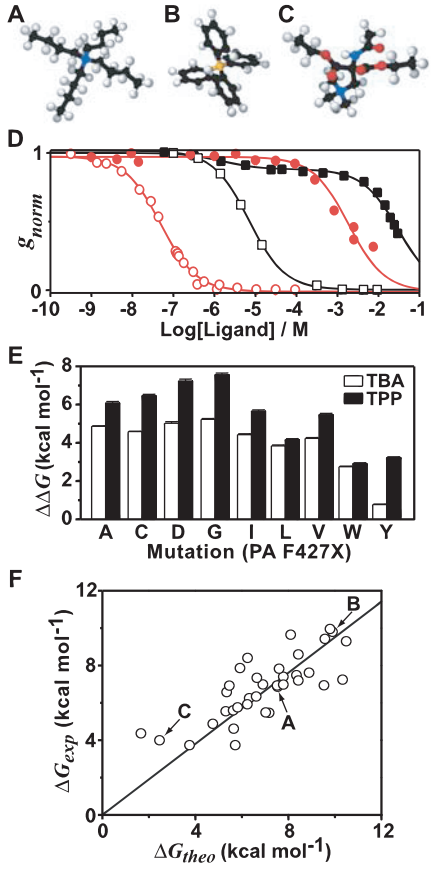

Fig. 3. QAP conductance block at the ϕ-clamp site. (**A**) TBA, (**B**) TPP, and (**C**) a hydrophilic analog of TBA (2-acetylamino-2,2-bis-ethoxy-carbonyl-ethyl)-trimethyl-ammonium, colored by atom: C (black), N (blue), O (red), H (white), and P (orange). (**D**) QAP ions were added symmetrically to the cis and trans compartments (Δψ = +20 mV, pH 5.5), and g_{norm} was recorded once QAP binding reached equilibrium. For TPP block, single-site binding models were fit for WT PA_{63} (red ○), K_D = 46 ± 2 nM (±SD), and F427A PA_{63} channels (red ●), K_D = 1.7 ± 0.2 mM. For TBA block, a single-site binding model was fit for WT PA_{63} (black □), K_D = 7.3 ± 0.3 μM, but a two-site binding model was required for F427A PA_{63} (black ■), such that the K_D values of the major amplitude (88%) and minor amplitude (12%) were 30 ± 2 mM and 1.5 ± 0.7 μM, respectively. (**E**) Binding free energy change, $\Delta\Delta G = RT \ln K_D^{Mut}/K_D^{WT}$, of TBA (white bars) and TPP (black bars) block for F^{427} mutants. (**F**) Model compound blocking studies of WT PA_{63} channels, performed as in (D). Experimental binding energies ($\Delta G_{exp} = RT \ln K_D$) were correlated to the expected binding energies (ΔG_{theo}) composed of solvation (ΔG_s) (*18*) and aromatic enhancement (ΔG_{aro}) energies as well as an offset, *c*, where $\Delta G_{theo} = \Delta G_s + \Delta G_{aro} + c$. $\Delta G_{aro} = \alpha n$, where α was fit to 0.7 ± 0.3 kcal mol^{-1} per aromatic ring, using the number of aromatic rings per compound, *n*. *c* was 0.8 ± 0.4 kcal mol^{-1} (table S1). The linear fit, $\Delta G_{exp} = \Delta G_{theo} \times m$ (35 compounds), had a slope, *m*, of 0.95 ± 0.03 and total error, σ_{SD}, of 1.2 kcal mol^{-1}. Arrows indicate compounds in (A), (B), and (C).

interactions, which occur when aromatic residues interact with cations through their delocalized, negative π-electron clouds (*17*).

We next examined a library of 35 quaternary ammonium and phosphonium ion (QAP) compounds to establish the nature of the ϕ-clamp binding interaction. Aliphatic QAP compounds (table S1) blocked conductance according to a solvent-accessible surface area solvation energy model (*18*); i.e., compounds with more hydrophobic surface blocked more effectively (Fig. 3F). Thus, a hydrophilic analog of TBA that is comparable in size, but functionalized with hydrophilic amide and ester groups (Fig. 3C), blocked 140-fold more weakly than TBA (table S1). We found that WT channels preferred tetraphenylphosphonium (TPP) (Fig. 3B) to TBA by 160-fold (Fig. 3D). Broadly across the QAP library, the ϕ clamp preferred aromatic moieties by ~0.7 kcal mol^{-1} per aromatic ring (Fig. 3F and table S1). Specifically, the conductance block observed for the polyaromatic, 4-aminoquinolone drug, quinacrine (*19*), was reduced ~1000-fold in F427A channels (fig. S3), indicating the ϕ-clamp site may be exploited in the development of channel-blocking drugs. Thus the correlation observed for the diverse QAP compound library (Fig. 3F and table S1) indicates that the ϕ clamp does not, in and of itself, recognize specific geometric or steric features of the substrates. Instead, the WT ϕ clamp recognizes substrates primarily by nonspecific hydrophobic interactions (*20*), although its negative π-clouds also contribute electrostatically through aromatic-aromatic, π-π and cation-π interactions.

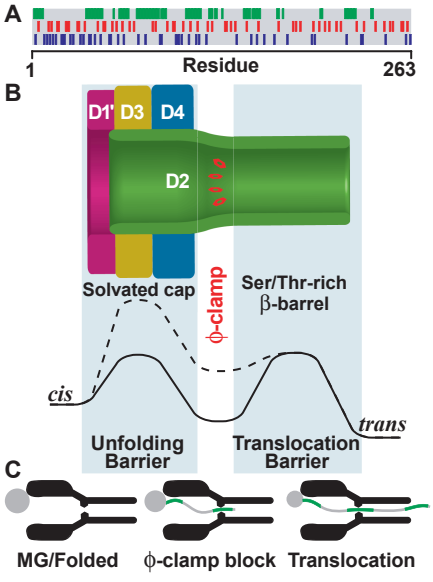

Fig. 4. A model of ϕ-clamp catalyzed protein translocation. (**A**) Chemical complexity of a PA_{63} substrate, LF_N, in which residues are colored by functionality: hydrophobic (green), greater than –1.75 kcal mol^{-1} in solvation energy (*18*) after applying a 10-residue running-window average; cationic (blue); and anionic (red). (**B**) The PA_{63} pore with a luminal ϕ-clamp site (red) is structurally imposed on an energy-well diagram for a hydrophobic stretch of polypeptide sequence from LF_N [see (A)]. The ϕ-clamp site is the anticipated well, separating the unfolding barrier on the cis side in the solvent-filled cap from a translocation barrier on the trans side in the solvophilic, Ser/Thr-rich β barrel. Energy diagrams are for WT and F427A PA_{63} (solid and broken lines, respectively), where the mutation simultaneously reduces the hydrophobic-mediated stabilization imparted by the ϕ-clamp site and raises the barrier to unfolding hydrophobic sequences from the protein substrate. (**C**) Intermediate states for a stepwise, Brownian ratchet unfolding and translocation mechanism, such that hydrophobically dense polypeptide segments (green) interact with the ϕ-clamp constriction.

In determining a model for translocation, we disfavored a priori relationships used to describe metal ion-conducting channels, because metal ion throughput (Fig. 1F) did not correlate with protein transport (Fig. 2, D and E), and the steric constraints imposed by the ϕ-clamp site did not impede protein translocation. The WT ϕ-clamp site should create a hydrophobic and steric energy barrier for bulky, hydrophilic, or charged residues in the protein substrate. Paradoxically, although channels containing narrower, aromatically lined ϕ-clamp sites were less ion conducting, they translocated LF_N orders of magnitude more rapidly than channels made wider, more hydrophilic, and more ion conducting at the ϕ-clamp site.

We therefore considered a chaperone model in which the ϕ-clamp's phenyl rings directly interacted with the translocating polypeptide. This view is supported, because the ϕ clamp forms a narrow iris (Fig. 1E) that can effectively grasp the translocating polypeptide chain (Fig. 2A, diagram). Furthermore, model compound studies indicate that the ϕ clamp recognizes substrates through the hydrophobic effect, enhanced by aromatic-aromatic, π-π, and cation-π interactions (Fig. 3 and table S1). Similarly, in the potassium ion channel from *Streptomyces lividans* (KcsA), a hydrophobic cavity defines the TBA blocking site and corresponds to a docking site for a hydrophobically dense peptide sequence (*21*). In globular proteins, like LF, hydrophobically dense peptide segments occur periodically along the translocating chain (Fig. 4A). As these segments unwind from the MG protein, they would be expected to bind favorably to the ϕ clamp, causing translocation to be blocked kinetically by the unfavorable hydrophilic barrier in the Ser/Thr-rich β barrel (Fig. 4B). Thus the ϕ-clamp energy well might be expected to hinder translocation, causing polypeptide segments bound at the site to "pause." However, as the ϕ-clamp site actually catalyzes polypeptide translocation, it must reduce some other larger barrier, such as the unfolding of the substrate protein. By analogy to the KcsA channel's selectivity filter, which provides sequential rings of hydrophilic carbonyl oxygen atoms that mimic the inner hydration shell of a K^+ ion (*22*), we propose that the ϕ-clamp site creates an environment that mimics the hydrophobic core of the unfolding MG protein. This would reduce the energetic penalty of exposing hydrophobic sequences to solvent or the hydrophilic lumen of the channel. The PA_{63} pore would thereby function as a Brownian ratchet, enabling the unwound leading segment of a translocating protein to move through the channel, and the trailing part of the protein to more readily unfold (Fig. 4C).

The results presented here show that PA_{63} is not merely a passive conduit through which proteins electrophorese; rather, it actively engages the translocating substrate via the ϕ clamp. This paradigm may be relevant to the functions of other polymer-translocating channels containing exposed hydrophobic sites, such as the "hydrophobic gasket" and "aromatic slide," identified in the structures of the protein secretase (*23*) and maltoporin (*24*) channels, respectively.

References and Notes

1. R. J. Collier, J. A. Young, *Annu. Rev. Cell Dev. Biol.* **19**, 45 (2003).
2. A. M. Friedlander, *J. Biol. Chem.* **261**, 7123 (1986).
3. C. J. Miller, J. L. Elliott, R. J. Collier, *Biochemistry* **38**, 10432 (1999).
4. R. O. Blaustein, T. M. Koehler, R. J. Collier, A. Finkelstein, *Proc. Natl. Acad. Sci. U.S.A.* **86**, 2209 (1989).
5. E. L. Benson, P. D. Huynh, A. Finkelstein, R. J. Collier, *Biochemistry* **37**, 3941 (1998).
6. S. Nassi, R. J. Collier, A. Finkelstein, *Biochemistry* **41**, 1445 (2002).
7. B. A. Krantz, A. D. Trivedi, K. Cunningham, K. A. Christensen, R. J. Collier, *J. Mol. Biol.* **344**, 739 (2004).
8. J. Wesche, J. L. Elliott, P. O. Falnes, S. Olsnes, R. J. Collier, *Biochemistry* **37**, 15737 (1998).
9. S. Zhang, E. Udho, Z. Wu, R. J. Collier, A. Finkelstein, *Biophys. J.* **87**, 3842 (2004).
10. We define the membrane potential as $\Delta\psi = \psi_{cis} - \psi_{trans}$, where $\psi_{trans} = 0$ mV. The cis side is the side to which PA_{63} and LF_N are added.
11. Single-letter abbreviations for the amino acid residues are as follows: A, Ala; C, Cys; D, Asp; E, Glu; F, Phe; G, Gly; H, His; I, Ile; K, Lys; L, Leu; M, Met; N, Asn; P, Pro; Q, Gln; R, Arg; S, Ser; T, Thr; V, Val; W, Trp; and Y, Tyr.
12. B. R. Sellman, S. Nassi, R. J. Collier, *J. Biol. Chem.* **276**, 8371 (2001).
13. Mutation of several other sites in domain 2 were also shown to block translocation, but these prevented pore formation (*12*, *25*).
14. B. Hille, *J. Gen. Physiol.* **51**, 199 (1968).
15. S. Zhang, A. Finkelstein, R. J. Collier, *Proc. Natl. Acad. Sci. U.S.A.* **101**, 16756 (2004).
16. R. O. Blaustein, A. Finkelstein, *J. Gen. Physiol.* **96**, 905 (1990).
17. N. Zacharias, D. A. Dougherty, *Trends Pharmacol. Sci.* **23**, 281 (2002).
18. L. Wesson, D. Eisenberg, *Protein Sci.* **1**, 227 (1992).
19. F. Orlik, B. Schiffler, R. Benz, *Biophys. J.* **88**, 1715 (2005).
20. W. Kauzmann, *Adv. Protein Chem.* **14**, 1 (1959).
21. M. Zhou, J. H. Morais-Cabral, S. Mann, R. MacKinnon, *Nature* **411**, 657 (2001).
22. D. A. Doyle *et al.*, *Science* **280**, 69 (1998).
23. B. Van den Berg *et al.*, *Nature* **427**, 36 (2004).
24. T. Schirmer, T. A. Keller, Y. F. Wang, J. P. Rosenbusch, *Science* **267**, 512 (1995).

25. M. Mourez *et al.*, *Proc. Natl. Acad. Sci. U.S.A.* **100**, 13803 (2003).
26. B. A. Krantz, R. A. Melnyk, R. J. Collier, A. Finkelstein, unpublished data.
27. D. B. Lacy, D. J. Wigelsworth, R. A. Melnyk, S. C. Harrison, R. J. Collier, *Proc. Natl. Acad. Sci. U.S.A.* **101**, 13147 (2004).
28. Materials and methods are available as supporting material on *Science* Online.
29. Translocation of LF_N (and full-length LF) was greatly accelerated when the pH on the trans side was greater than that on the cis side (*26*).
30. R.J.C. is cofounder, member of the scientific advisory board, and equity holder in PharmAthene, Inc., a startup company that investigates countermeasures against anthrax and other bioterrorism agents. We thank K. J. Oh for EPR data acquisition; R. Ross at the New England Research Center of Excellence Biomolecule Production Core as well as R. Pimental, L. Greene, and H. Lin for their assistance in purifying and generating PA mutants; and W. Hubbell, T. Sosnick, and A. Johnson for useful discussions. This work was supported by a National Research Service Award fellowship, AI062204 (B.A.K.), and NIH grants, AI022021 (R.J.C.) and GM29210 (A.F.).

Supporting Online Material
www.sciencemag.org/cgi/content/full/309/5735/777/DC1
Materials and Methods
SOM Text
Figs. S1 to S3
Tables S1 and S2
References and Notes

11 April 2005; accepted 2 June 2005
10.1126/science.1113380

Genetic Tracing Shows Segregation of Taste Neuronal Circuitries for Bitter and Sweet

Makoto Sugita* and Yoshiki Shiba

The recent discovery of mammalian bitter, sweet, and umami taste receptors indicates how the different taste qualities are encoded at the periphery. However, taste representations in the brain remain elusive. We used a genetic approach to visualize the neuronal circuitries of bitter and sweet tastes in mice to gain insight into how taste recognition is accomplished in the brain. By selectively expressing a transsynaptic tracer in either bitter- or sweet and/or umami–responsive taste receptor cells, and by comparing the locations of the tracer-labeled neurons in the brain, our data revealed the potential neuronal bases that underlie discrimination of bitter versus sweet.

The gustatory system is primarily devoted to a quality check of food, while at the same time detecting nutrients and avoiding toxic substances. The initial step in taste perception takes place at the apical end of taste receptor cells, tightly packed into taste buds of the oral epithelium. The cells express taste receptors, which are responsible for detecting and distinguishing among sweet, bitter, salty, sour, and umami stimuli (*1*). In mammals, bitter and sweet and/or umami are the two main taste modalities evoking aversion and attraction, respectively. Humans also express pleasure for sweet taste but displeasure for bitter taste. On the other hand, mammals learn to reject a tastant if this tastant is associated with subsequent visceral malaise (*2*). Therefore, it is likely that the mammalian gustatory system is an excellent system to address the question of how emotion interacts with cognition and memory. To decipher rationally the underlying molecular, cellular, and system mechanisms, it is first necessary to understand and to compare precisely the contrastive neuronal circuitries that process and integrate the information of aversive and attractive taste modalities in the whole brain.

Department of Physiology and Oral Physiology, Graduate School of Biomedical Sciences, Hiroshima University, Kasumi 1-2-3, Minami-ku, Hiroshima 734-8553, Japan.

*To whom correspondence should be addressed. E-mail: sugisan@hiroshima-u.ac.jp

Bitter tastants are detected by members of a family of 30 different G protein–coupled receptors (GPCRs), the T2Rs (*3*–*5*). Sweet and umami tastes are substantially mediated by a small family of three GPCRs (T1R1, T1R2, and T1R3). T1R2 and T1R3 combine to function as a sweet receptor, whereas T1R1 and T1R3 form the umami receptor, which detects glutamate (*6*, *7*). Sweet, umami, and bitter receptors appear to be expressed in distinct populations of taste cells that operate independently of each other to trigger taste recognition (*6*, *8*–*10*). The receptor cells are innervated by afferent fibers that transmit information to the gustatory cortex through synapses in the brain stem and thalamus (*11*). How is taste information processed in the central nervous system, while it is discriminated and as it evokes the emotional and behavioral responses such as aversion and attraction? We applied a genetic approach to visualize the neuronal circuitries of bitter and sweet-umami taste by using the taste receptor genes and the plant lectin WGA as molecular tools. Injected lectin proteins are an effective tracer for transsynaptically delineating the wiring patterns in the central nervous system (*12*–*14*). Furthermore, the genetic approach using the WGA transgene, expressed under the control of specific promoter elements, is a powerful tool for tracing selective and functional neuronal circuitries originating from a specific type of neuron (*15*, *16*).

We prepared transgenic mice in which the transsynaptic tracer WGA, C-terminally truncated and fused by the fluorescent protein (tWGA-DsRed), was coexpressed with selected taste receptors. The transgene for tracing the bitter taste neuronal circuitries is shown in Fig. 1A. We selected the promoter element of the mT2R5 gene, reported as a receptor for cycloheximide (*5*), to drive tWGA-DsRed expression in bitter receptor–expressing cells. In phospholipase Cβ2 (PLCβ2)–deficient mice, which lack sweet, amino acid, and bitter taste reception, the PLCβ2 transgene, expressed under the control of the mT2R5 promoter, rescued the response to multiple bitter compounds, but not to sweet or amino acid taste (*8*, *10*). The findings support not only that taste receptor cells are not broadly tuned across these modalities, but also that the mT2R5-expressing cells coexpress the multiple T2Rs and are capable of responding to a broad array of bitter compounds. The transgene was constructed by connecting the promoter element of mT2R5, the fusion constructs of mT2R5 with green fluorescent protein (mT2R5-GFP) and tWGA-DsRed, which intercalated the internal ribosome entry site (IRES), and the polyadenylation signal (Fig. 1A). To test whether a part of the transgene works, Cos7 cells and HEK293 cells were transiently transfected with the construct, in which the upstream region of mT2R5 was replaced by the cytomegalovirus (CMV) promoter (Fig. 1B). The fusion proteins of mT2R5-GFP and tWGA-DsRed were expressed in these cells (Fig. 1B), which suggested that the transgene produces a bicistronic mRNA from which mT2R5-GFP and tWGA-DsRed are independently translated. Furthermore, the tWGA-DsRed fusion protein was associated with the intracellular granule–like structures of cultured cells. The mT2R5-GFP fusion protein was localized in the cell surface membrane (Fig. 1B). In addition, fura-2 calcium imaging of HEK293 cells, cotransfected with T2Rs-GFP and Gα15, revealed that fusion of GFP to the C terminus of T2Rs does not affect the receptor function (*17*).

First, to verify the expression patterns of the endogenous mT2R5 and the transgene in the transgenic mice (mT2R5-WGA), we performed in situ hybridization using the 3′ untranslated region of mT2R5 and the GFP-coding region as probes for double-label fluorescent detection. The cells expressing the